Transmission $(e,2e)$ coincidence measurements of thin evaporated carbon, graphite, and aluminum–aluminum oxide foils

P. Hayes, J. F. Williams, and J. Flexman
Physics Department, The University of Western Australia, Perth, Western Australia 6009, Australia
(Received 6 June 1990)

Symmetric transmission $(e,2e)$ coincidence data are presented from the valence region of evaporated amorphous carbon, graphite, and aluminum–aluminum oxide thin (between 100 and 200 Å) foils. The count rate of this technique, within the plane-wave-impulse approximation, is directly proportional to the spectral momentum density. The data were accumulated at a probe energy of 7.5 keV with typical energy and momentum resolutions of 4.5 eV and 0.9 $Å^{-1}$ full width at half maximum (FWHM), respectively. The aluminum oxide foil was investigated close to 0 $Å^{-1}$ binding momentum with an improved energy resolution of 1.5 eV FWHM. The resolved electron states are related to the S and P nature of the valence electrons in these materials with a small atomic number. The similarity between amorphous carbon and graphite suggests that the amorphous sample was largely graphitically bonded. The results are discussed with special attention paid to the short, electron mean free paths within the solid samples.

I. INTRODUCTION

Transmission $(e,2e)$ coincidence measurements on solid foils give an experimentally well-defined knockout reaction that can be directly related to the electronic structure of the target. The results of this paper were accumulated from amorphous carbon, graphite, and aluminum oxide with the bulk of the data acquired at momentum and energy resolutions of 0.9 $Å^{-1}$ full width at half maximum (FWHM) and 4.5 eV FWHM, respectively. The carbon data were accumulated from the valence band, i.e., from 0 to about 40 eV, with the momenta measured from -4.9 to 4.4 $Å^{-1}$ in steps of about 0.8 $Å^{-1}$. We report also improved energy resolution measurements at 1.5 eV FWHM with an aluminum foil and compare them with earlier data from this laboratory.[1] Some binding-energy spectra are extended below the valence region by about 80 eV for a more thorough evaluation of satellite structure.

The $(e,2e)$ probing reaction uses an electron of known momentum to knock out a bound electron: the scattered and ejected electrons are then detected simultaneously with well-defined momenta. By collecting the electrons in coincidence, both outgoing electrons can be identified with a single scattering event. In the single-particle-impulse approximation the coincidence count rate is directly proportional to the spectral momentum density $A(\varepsilon,\mathbf{q})$, i.e., the probability of finding a solid-state electron with energy ε and momentum $\mathbf{q}$. The function $A(\varepsilon,\mathbf{q})$ maps out the electronic band contours in the repeated-zone scheme. This explicit information is currently available only from the kinematically complete $(e,2e)$ measurement. Other experimental methods, such as Compton scattering and angle-resolved photoemission, measure parts of this distribution and integrate in some way over an unmeasured parameter involving either energy or momentum. The coincidence filtering of the scattered information dramatically increases the time for the experiment. This fact in combination with the short, electron-scattering mean free paths in a foil have limited earlier data collection to broad sampling areas of the valence-core levels in a solid.[2] The measurement by Ritter *et al.*[3] on amorphous carbon was the first experiment to resolve valence structure, with quoted energy and momentum resolutions of 6 eV and 0.6 $Å^{-1}$ FWHM, respectively, the improvement being largely due to an increased probing energy of 25 keV. That group then followed with an archetypal experiment[4] on a single-crystal graphite sample, a material that is well described by theory. Even though the data showed rather large experimental uncertainty, the broad structure agreed both in intensity and position with the spectral momentum density calculated in the plane-wave-impulse approximation. This indicated that the basic theory was sound and could be extended to less well understood systems such as amorphous solids, a group of materials that are presently more suited to the transmission coincidence method than perhaps single crystals.

We begin with a brief account of the $(e,2e)$ scattering dynamics and plane-wave-impulse theory. This is followed by sections that discuss theoretical solid-state extensions and the influence of multiple scattering arising from independent single-channel collisions. Symmetric coincidence data for evaporated carbon, graphite, and evaporated aluminum–aluminum oxide films are then studied at the significantly lower incident electron energy of 7.5 keV. This approach decreases systematic errors that occur with higher-energy data collection. The present data are compared with Ritter's data, for the first comparison of independent $(e,2e)$ coincidence measurements on similar solid targets, under conditions where the energy of the probing electron should have no effect on the information content if the plane-wave impulse approximation remains valid. We also analyze the spectra

to take account of the increased multiple scattering that occurs at the lower probing energy. A similar comparison is performed with graphite, while the aluminum–aluminum oxide data are related to previous poorer resolution results.

II. SCATTERING DYNAMICS

The $(e,2e)$ measurement is kinematically complete. The incident electron (subscript 0) is projected at the target with defined energy and momentum E_0 and $\mathbf{k}_0$. The scattered (subscript s) and ejected (subscript e) electrons are detected with energies (E_s,E_e), momenta $(\mathbf{k}_s,\mathbf{k}_e)$ at angles (θ_s,θ_e) with respect to the straight-through beam. The highest-energy electron of the two outgoing electrons denotes the scattered electron. The measurement of energy and momenta of all participating particles, for each scattering event, yields direct information about the scattering process and the initial state of the bound electron. Specific electron coincidence experiments restrict themselves to a small portion of the total phase space. Study of the atomic scattering dynamics is normally performed[5] at low electron energies to increase the Coulomb interaction. At high energies, by contrast, the results represent a measurement of the ejected electron's spectral momentum density before ionization, given the assumption that the electron is not strongly correlated to other bound electrons. The selection of a specific state in a crystal follows from the reaction's energy and momentum conservation relations of $\varepsilon=E_0-(E_s+E_e)$ and $\mathbf{q}=\mathbf{k}_0-(\mathbf{k}_s+\mathbf{k}_e)$ where ε and $\mathbf{q}$ are the selected energy and momentum. As shown by Levin *et al.*[6] the calculated momentum $\mathbf{q}$ is related to the crystal wave vector $\mathbf{k}$ in the first Brillouin zone by the addition of a reciprocal-lattice vector $\mathbf{B}$, where $\mathbf{q}=\mathbf{k}+\mathbf{B}$. For high-momentum-transfer conditions the scattering probability has been shown theoretically and experimentally to be directly proportional to the electron spectral momentum density $A(\varepsilon,\mathbf{q})$. The differential cross section using the frozen-orbital assumption[7]

$$\frac{d^5\sigma}{d\Omega_s d\Omega_e dE_s}=4\pi^3 n\frac{k_s k_e}{k_0}F_{e,e}\,A(\varepsilon,\mathbf{q})\ , \tag{1}$$

where n is the number of valence electrons per unit volume and $F_{e,e}$ is the free–electron-electron Mott scattering term. An additional correction term that depends on the band dispersion, not included here, is close to unity for high-energy and free-electron or atomiclike bands.

To satisfy the high-momentum-transfer conditions, a symmetric high-energy scattering geometry is chosen. In the symmetric transmitted geometry, the outgoing electrons are detected from the exit side of the foil at equal energies $(E_s=E_e\approx E_0/2)$ and angles $(\theta_s=\theta_e)$ coplanar to the incoming electron beam. The momentum vector of the bound electron is then studied perpendicular to the thin target and is approximately given by

$$\mathbf{q}=(\sqrt{2}\cos\theta_s-1)\mathbf{k}_0\ . \tag{2}$$

The terms preceding the spectral momentum density of Eq. (1) tend to a constant for varying measured momentum as the energy of the experiment is increased. For symmetric experiments the Mott term becomes equal to the Rutherford differential cross section, which is approximately given by $[k_0(k_0/2-q)]^{-2}$. For the primary energy of 7.5 keV ($k_0=44.5$ Å^{-1}) used here, the modulation in intensity from $\mathbf{q}=-3$ to 3 Å^{-1} relative to $q=0$ Å^{-1} is from -22% to 34%. Apart from this slow variation, the coincidence count rate is proportional to the momentum density in the plane-wave-impulse approximation.

In principle, the $(e,2e)$ technique can define the momentum direction and magnitude of the momentum for the measured bound state. Other methods also exist to determine the momentum density, but they either integrate over the direction in some way or require other knowledge of the bound state. For example, Compton profiles, collected through the excitation of solid-state electrons via high-energy photons or electrons (HEEIS), give an integrated momentum density that reflects the valence band as a whole. Two of the most widely used techniques to map out band structure are angular-resolved ultraviolet spectroscopy and secondary electron emission. These approaches are able to detail the band structure that includes unoccupied conduction-band states. However, they require prior knowledge of the band structure to match peaks seen in the electron distribution. The principle applied is momentum conservation throughout the scattering process in the direction in the crystal plane. This procedure selects a relatively well-defined value of the momentum, but its value can be determined only if further information is available on the final state.

III. ADDITIONS TO THEORY

The theory assumes that the incoming electron interacts only with the knocked out electron, i.e., the single-particle approximation. As Levin *et al.*[6] explain, the coupling of electrons in s and p states is expected to be weak and the approximation would remain valid. For the narrower d and f bands, correlation is significant and the configuration of the final state will become important. The configuration of the final state in the atomic case leads to satellite peaks in the binding-energy spectrum, as seen in the argon spectrum for which the inner 3s valence manifold divides into several state, with the momentum density curves being approximately equivalent in shape. In a solid, coupling may also exist between the hole and the electron plasma, leading to the creation of a plasmaron state, as described in a series of papers by Lundquist.[8] The created hole is rapidly screened (10^{-16} sec) through the superposition of plasmons. This may lead to a satellite structure in the momentum density that disperses with momentum. The theory was formalized[9–11] with respect to the $(e,2e)$ experiment, though the hole was considered localized, i.e., the knockout reaction of a deeply bound electron. From earlier experimental studies, an intense portion of the structure following the valence region of a solid in the $(e,2e)$ binding-energy

spectrum was attributed to the plasmaron state. In more recent studies, the tail has been shown to consist mainly of energy straggling collisions from the primary event, though the plasmaron may exist at a reduced intensity.

The earlier theory also assumes that the high-energy electrons are well represented by plane waves. In an extended periodic potential this approximation may need modification to a linear combination of Bloch waves. Allen *et al.*[12] predict, through self-interference effects arising from elastic reflections in a local environment, that the collision event can become strongly localized within the crystal unit cell. A similar weak result is seen in the extended energy-loss fine-structure (EXELFS) studies, where nearest-neighbor distances can be extracted from oscillations in the scattered energy tail. Since the $(e,2e)$ cross section is proportional to the product of three independent probability densities, it may show some site-dependent tendencies. The strength of diffraction phenomena has not been demonstrated theoretically or experimentally for any solid sample, but is expected to decrease exponentially with increasing electron momentum.

IV. MULTIPLE SCATTERING

Multiple scattering occurs when the incoming or outgoing electrons are either scattered elastically or inelastically one or more times. The number of scatterings depends on the cross section of the possible interactions, the foil thickness, and the beam energy. To reduce the multiple-scattering contribution the free-standing foil targets are made as thin as possible and the beam energy is raised as high as practicable to increase the mean free paths of the electrons.

The evidence of multiple scattering is seen in the coincidence binding-energy tail below the primary valence structure. The broad peak of this energy distribution depends on the number of average collisions per coincidence event and the average energy lost per collision. The valence structure is only affected in form by single inelastic collisions, since higher numbers of collisions push these events to lower energies. The deeper band structure then rests on a background of essentially single-channel collisions from the preceding band states.

The major inelastic-scattering mechanism is the creation of a volume plasmon,[13] a collective oscillation of the valence electrons. The energy required to produce a plasmon depends on the electronic configuration and density of the material. For example, the free-electron metal aluminum has a sharp volume plasmon at $E_p = 15$ eV, while for amorphous carbon the plasmon peak has a broader complex structure that peaks at $E_p = 26$ eV. The electron is deflected through a small angle, less than the plasmon critical momentum transfer of order 1.3 Å^{-1}, after plasmon formation. In relation to the coincidence spectra, the plasmon features are expected to contribute to the spectra at multiples of the plasmon energy below some real valence feature. The valence structure will be reproduced but convoluted with the multiple plasmon line shape. In the case of carbon, the single plasmon width is about 24 eV, which would smear the satellite form considerably. For the energies used in this experiment the mean free paths are similar to the foils' dimensions: for aluminum[14] at 3.75 keV, $\lambda_p = 110$ Å, and 7.5 keV, $\lambda_p = 200$ Å; and for carbon[15] at 3.75 keV, $\lambda_p = 62$ Å, and 7.5 keV, $\lambda_p = 110$ Å. From Poisson statistics there is unfortunately a high probability that at least one plasmon will be created in the solid per reaction. Other energy-loss features also contribute to a "smearing" function, but they have cross sections about an order of magnitude smaller, such as individual electron excitation, or they require energy losses greater than the valence energy range, such as inner-shell excitation.

Elastic scattering has similar mean free paths to plasmon scattering and as the atomic number of the materials increases it becomes the dominant scattering mechanism. In the amorphous solid, elastic collisions will cause the spectral momentum density to broaden along the momentum axis. For a crystalline solid, elastic scattering is allowed only in the Bragg directions: in particular, no scattering would occur with the measured momentum inside the first Brillouin zone. Outside the zone, the spectral momentum density may exhibit rapid changes when either of the electrons is Bragg reflected.

An evaluated smearing energy function of straggling collisions[16] can be used to deconvolute the background to yield a clearer picture of the deeper band structure. This function should also include the angular spread resulting from elastic and inelastic events. A full account of angular spread was not attempted here because the data points along the momentum axis are sparse and therefore difficult to deconvolute without introducing noise. The correction for angular spread is expected to be small since the leading valence structure is reasonably smoothly varying at the momentum resolution used here, when compared to the deflection from an energy-loss event that is sharply peaked in the forward direction [$\Delta\theta$ (half intensity) $= \pm 0.5°$ for aluminum at 3.75 keV]. The elastic events, similarly, are forward scattered and contribute to a spread in the primary momentum structure. Elastic scattering in noncrystalline carbon or aluminum is approximately described[17] by a modified screened Rutherford function. From this function and experimental measurement, only a small percentage of the electrons scattered elastically remain within the field of view of the analyzers. For instance, electrons scattered from carbon at 3750 eV have a 2% chance of remaining within $\pm 1.2°$ of the incoming direction. As a first approximation, elastic scattering is assumed to eliminate the coincidence event from detection. A more meaningful isotropic simulation of elastic scattering with experimental energies and foil thickness did suggest that the form of the momentum distribution near the peak measured momentum was unaltered. The elastic scattering, in general, allows a small fraction of higher-momentum states to scatter into the lower-momentum data. For carbon (120 Å thick) the simulation gave a slowly decreasing background from the transmitted peak to about 4.0 Å^{-1} below it. With the assumption of a uniform momentum density, the elastic scattered background intensity was about 18% of the total collected coincidence events. For high measured momentum, the detected scattered intensity will be reduced by the convoluted momentum density which de-

creases by orders of magnitude over this interval. For states that tend to a node close to zero measured momentum, multiple scattering may introduce a small blending of band structure over the above interval.

By combining the scattering mechanisms into a Monte Carlo simulation a smearing function in energy can be readily computed. The elastic and inelastic mean-free-path parameters and the profiles of the primary energy-loss structure used in the simulation were verified against single-channel energy loss and total transmission current measurements at near straight-through angles. For amorphous carbon the single-channel energy-loss distribution is shown in Fig. 1, along with a calculated result. The simulated curve takes into account the aperture size of the detectors, the plasmon shape, and the mean free path. The shape of the theoretical Drude-summed plasmon curve[15] was modified to give a better match to the measured energy-loss distribution, which brings it closer to the optically measured profile. The only free parameter was the thickness of the foil. The agreement between data and the simulated result is good.

The coincidence smearing function is evaluated only to fit the energy scale. The effect of elastic scattering, within the above approximation, is to change the uniform spatial distribution of detected coincident events within the solid, to a preferential weighting of events occurring close to the exit side of the foil. The smearing function folded with the experimental energy resolution is deconvoluted from the coincidence binding-energy data using the iterative van Cittert[18] technique. The deconvolution process was terminated when the χ^2 probability between data and the reconvoluted ideal function approached unity.

Apart from the decline in the clarity of the spectrum, multiple scattering also reduces the total number of detectable coincidence events. The optimum theoretical foil thickness can be found approximately by considering, as a function of increasing thickness, the linearly increasing number of target centers and the exponentially declining probability of a coincident event that does not suffer any single-channel events. At a primary beam energy of 7.5 keV the function is peaked at an optimum thickness of about 20 Å for both aluminum and carbon foils, with approximately 35% of events escaping unscattered. For an experimental foil thickness of about 100 Å, the unscattered percentage drops to about 3%, a dramatic reduction in the expected coincidence count rate. The asymmetry in the number, energy, and escape angle of the incoming and outgoing electrons, as mentioned earlier, weights the distribution of unscattered coincidence events close to the exit side of the foil. The point in the foil beyond which 50% of the events that do escape unscattered can be found simply from Poisson statistics as

$$0.5=[1-\exp(-x/\Lambda)]/[1-\exp(-T/\Lambda)]\ , \qquad (3)$$

where $1/\Lambda=1/\lambda_0-2\sqrt{2}/\lambda_s$, and where x is the depth from the front of the foil, T is the foil thickness, and λ_0 and λ_s are the total mean free paths (mfp's) for the incoming and scattered electrons. The escaping electrons leave the foil symmetrically at 45°. Under our experimental conditions, the 50% point for most foil types will lie within 20 Å of the exit side of the foil. For example, amorphous carbon has combined elastic and inelastic mfp's of about 30 and 56 Å at beam energies of 3.75 and 7.5 keV, respectively. This gives for carbon (110 Å thick) a 50% point of 9 Å from the exit side of the foil. Therefore, the $(e,2e)$ technique at these energies becomes preferentially sensitive to surface electron states.

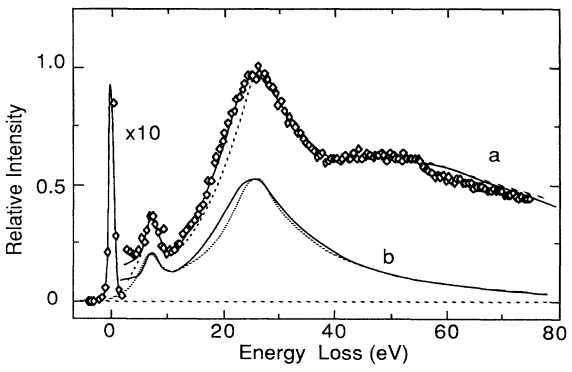

FIG. 1. A characteristic energy-loss spectrum at 0° of thin (110 Å) evaporated carbon is shown for an incident energy of 3750 eV. The solid and dotted lines are the Monte Carlo results using the Drude plasmon-loss function of Ashley *et al.* (Ref. 15) (— — —) and a modified profile (——), which are shown separately in curves *b* and fitted to the spectrum in curves *a*.

V. MEASUREMENT OF ENERGY AND MOMENTUM

The experimental setup has been described in detail elsewhere.[1,19] Briefly, the apparatus consists of an electrostatic electron gun (0.2–10 keV) and two electrostatic hemispherical electron analyzers, with two three-element input lenses and entrance apertures, which momentum select the two outgoing electrons. A Faraday cup is set at the straight-through position to collect the unscattered current. The analyzers rotate independently about the interaction region. The electrons radially dispersed by the analyzers' electrostatic field are detected over a range of energies by position-sensitive microchannel plate assemblies (MCP's) from Surface Science Laboratories. Pairs of electrons arising from the same knockout event and by-chance coincidence are selected through coincidence-timing electronics. These events gate the recording of the electrons' energy in the appropriate data acquisition bin in a LeCroy 3500M microcomputer.

Typically, the system had a background pressure of 10^{-8} Torr when accumulating data from a thin solid target with an incident electron-beam energy of 7.5 keV and a current of 0.1 μA into a spot of 0.2-mm diam. Higher currents were found to cause a rapid deterioration in the free-standing aluminum foils. The total detected count rate was symmetric in each analyzer (within 10%) and was limited to moderate frequencies of between 5 and 20 kHz, so as not to degrade the response of the position-sensitive detectors. For aluminum targets the count rate was constrained by the maximum current dosage, while for carbon, which was stable at a higher dose, the count

rate itself became the limiting factor.

The events acquired from one detector were uniformly spread in energy along a slit pattern (15×1 mm^2). The slit is logically divided into 20 bins through the computer program, each bin representing a different energy. Real and by-chance coincidence events were accumulated between all combinations of the 20 bins in each detector giving a grid of 400 coincidence channels. This grid was reduced to a binding-energy spectrum through combining channels that represent equal binding energy. That gave a 39-point coverage of the simultaneously acquired energy range.

The energy and momentum resolutions are found experimentally by performing initial experiments on argon-gas valence states. The gas is passed through a 0.5-mm-diam nozzle located 3 mm above the interaction region. The total-energy resolution of the system is dependent on the range of energies to be simultaneously acquired across the MCP's. Typically, this interval was set wide enough to adequately cover the valence-band region, 50 eV. A typical binding-energy curve for an incident energy of 7.5 keV is shown in Fig. 2. The measured energy resolution of 4.5 eV FWHM agreed with predictions based on the analyzer dimensions and electrostatic field strengths. The momentum resolution was determined by an angular correlation measurement of the argon $3p$ and $3s$ ion states as shown in Fig. 3. The theoretical calculation of momentum resolution is subject to the angular acceptance of the analyzers and the divergence of the incoming electron beam, about 0.3° FWHM. The contribution from the analyzers is found by numerically integrating over the pair of symmetric circular apertures

$$\Delta q \approx 0.43 k_0 \Delta\theta \ , \tag{4}$$

where $\Delta\theta$ is the small pencil angle in radians from the target to one analyzer. For small q, the resolution narrows because the analyzers accept positive and negative momenta of the same magnitude in the beam direction.

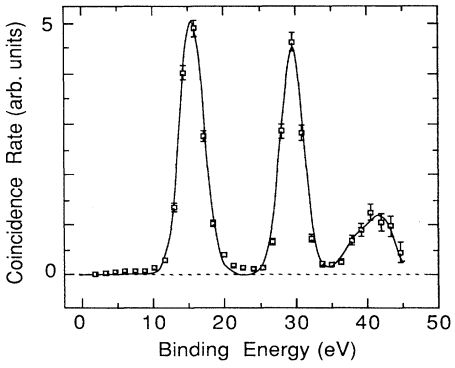

FIG. 2. The coincidence binding-energy distribution of argon gas collected at 7.5 keV at an energy resolution of about 4.5 eV FWHM. The first peak is the $3p$ ion state (15.76 eV), while the trailing peaks form the $3s$ manifold, the largest ion state occurring at 29.3 eV.

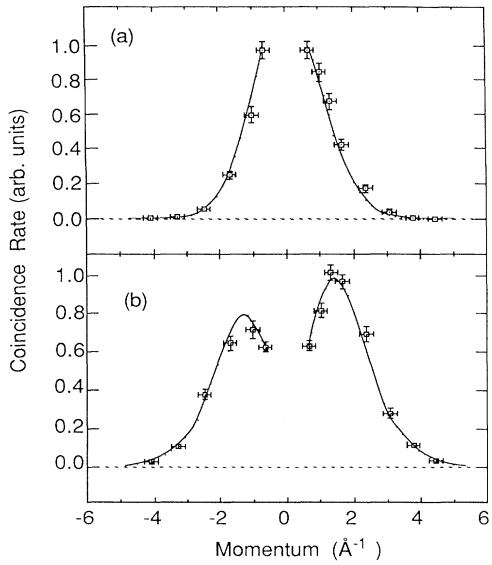

FIG. 3. The angular correlation data of (a) the $3p$ and (b) the $3s$ ion states (29.3 eV) at 7.5 keV. Both theoretical curves have been convoluted with a system resolution, at 0 Å^{-1} binding momentum, of 0.9 Å^{-1} FWHM.

The resolution improves to about $0.27k_0\Delta\theta$ at $q=0$ Å^{-1}. The acceptance angle of the analyzers was varied with two input aperture sizes of ±1.2° and ±0.5°, which gave total resolutions of 0.9 and 0.4 Å^{-1} FWHM, respectively.

The momentum spread accepted by the entrance apertures of the analyzers causes the peak measured momentum as set by Eq. (4) to shift. The corrected momentum equation for an isotropic target is approximately

$$q_c \approx (\mathrm{sgn} q_0)[q^2+0.125(k_0\Delta\theta)^2]^{0.5}k_0 \ . \tag{5}$$

Equation (5) indicates that to obtain a measurement of $q_c=0$ Å^{-1} the angular resolution of the analyzer must approach zero. With the above resolutions the momentum measurement at $\theta_s=45°$ is not the ideal $q=0$ Å^{-1} but a finite momentum. The effect is especially noticeable in the case of the measurement of a P state as shown in Fig. 3(b). Here the intensity is changing rapidly as a function of momentum near $q=0$ Å^{-1} with an ideal sharp drop to a node.

There are a number of sources of systematic error. The magnitudes estimated below are maximum values. Systematic errors arise in the absolute momentum measurement through the limit of positioning the electron beam at the central interaction region to within ±0.2 Å^{-1} with the main component in the plane of the foil and the limit of alignment of the analyzers of ±0.1 Å^{-1}. The energy scale is referenced to the $3p$ state of argon of 15.76 eV with a maximum error of ±0.75 eV within which the zero of the binding-energy scale shown in later figures is equal to the Fermi energy. The voltage supplies were stabilized so that the drift in binding energy was less than ±0.5 eV.

VI. TARGET PREPARATION

Thin amorphous carbon and polycrystalline aluminum foils were prepared through vacuum evaporation onto a soluble substrate. The substrates used were room-temperature high-quality glass slides coated with Decon-90 detergent. To prepare a uniform coating, the Decon-90 is diluted with distilled water (1 part in 100) and the slides dipped into the solution and then allowed to dry in air. The advantage of this substrate is that the foils readily release from the glass slide and that Auger electron spectra indicate that the Decon 90 does not appear to adsorb to the surface of the target.

Evaporation is carried out in a liquid-nitrogen trapped vacuum system at a base pressure of about 10^{-6} Torr. The carbon is evaporated from two spectroscopically pure rods of carbon through intense local heating produced by an arcing current at a poor point contact. The aluminum targets were made by evaporating 99.9% pure aluminum from a cleaned wire tungsten filament. Once deposited, the foils are floated free of the glass slides in a bath of distilled water. They are then transferred to a second bath for rinsing and picked up on an annular ring and dried in air. The thin foils used in this study were microscopically free of holes, and flat, stretched over a 2-mm-diam hole through each target washer. The foil thickness was estimated to within 20% from helium-neon laser transmission readings and *in situ* transmitted single-channel energy-loss spectra.

X-ray emission and Auger-electron-spectroscopy measurements suggest that the major contaminants in the case of aluminum are carbon and oxygen. Tungsten was present but in quantities less than 0.1%. The Auger tests suggested that carbon was largely deposited in the first few monolayers on each side of the foil. The oxygen was thought to be bonded in the form of the aluminum oxide. By exposing the aluminum foil to the atmosphere and the water bath a stable amorphous oxide layer forms at the surface of the foil to a depth of 15 to 30 Å. Since both sides of the foil oxidize, the target, which was typically about 120 Å thick, had a composition that was considered an equal combination of polycrystalline aluminum metal and amorphous oxide.

The graphite samples were prepared[4] by the "scotch-tape method." A pyrolytic graphite sample was carefully cleaved into thinner planes by gluing to each side of the thin sample, paper grips, then prying them apart. The division process was repeated until the sample became transparent ($>70\%$) over an area greater than 1 mm.^{2} The sample was then floated free by dissolving the glue, cleaned in subsequent baths of hot distilled water, and mounted on a target washer. To further thin the sample the technique of plasma etching was applied. A gas discharge was started between an anode and the sample in a gas mixture of argon (80%) and oxygen (20%) which reactively etched the exit surface of the sample. The etching rate was monitored by the transmission of a laser beam through the sample. It has been shown,[4] through a comparison with Raman-scattering measurements, that plasma etching does not significantly disrupt the crystal order at the surface.

The structures of the foils were verified by transmission electron-diffraction measurements using a 200-keV electron microscope. The evaporated carbon foils revealed only weak diffraction, with diffuse rings corresponding to its amorphous nature. The sample produced the same pattern independent of orientation relative to the transmitted beam, which indicated that the substrate had no bulk ordering effect of the sample in the plane of the foil. The thin targets of aluminum were composed of small crystallites whose orientation was random over a wide beam sampling diameter. The diffraction pattern's low-order rings matched that of aluminum metal, with no evidence of any crystalline contamination. The amorphous oxide layer was not apparent in this exploration. The graphite sample showed a uniform hexagonal spot pattern corresponding to the c axis orientated perpendicular to the slab. The pattern, however, did exhibit rotation as the sample traveled under the electron beam, that is, the crystal was composed of large crystallites that were rotated about the foil perpendicular relative to each other. Large numbers of dislocations were seen at the boundaries.

VII. RESULTS

A. Evaporated carbon

The amorphous carbon results shown are from a single sample with an estimated thickness of 110 Å. The investigation of other samples with similar thickness was found to give identical results at $\theta_e=\theta_s=45°$. The data plotted in Fig. 4 were acquired at a beam energy of 7.5 keV, with momentum and energy resolutions of 4.5 eV FWHM and 0.9 Å^{-1} FWHM, respectively. With the analyzers stationed at 45° and an incident electron current of 380 nA, the real coincidence count rate was about 3 counts/sec into a coincidence window set 5.6 nsec wide. The total background coincidence rate was about 6.5 counts/sec into a timing window 110 nsec wide defined around the coincidence window. It is noted that the "quality" of the experiment from a statistical viewpoint improves as the coincidence window (resolving time) decreases and as the ratio of the coincidence window to the background coincidence window decreases.[20] The energy of the system remained fixed during the 11-day collection time with the measured momentum swept cyclically. Periodically the 45° data were analyzed and compared to earlier spectra in the same run to identify long term drifts. No significant differences were identified. Spectra were also collected at order-of-magnitude lower beam currents to verify that differential charging was not occurring in the foil. These spectra were identical to those collected at the higher currents.

The experimental data revealed two distinct peaks in the valence region. At the analyzer's detection angles of 45°, the maximum datum points of these peaks are located at 12.8 and 26.5 eV, respectively. The relative difference in energy of 13.7 eV corresponds closely to that measured by Ritter *et al.*[3] for their amorphous carbon target experiments of 13 eV at their measured $q=1$ Å^{-1}. At their higher-beam energy of 25 keV with resolutions

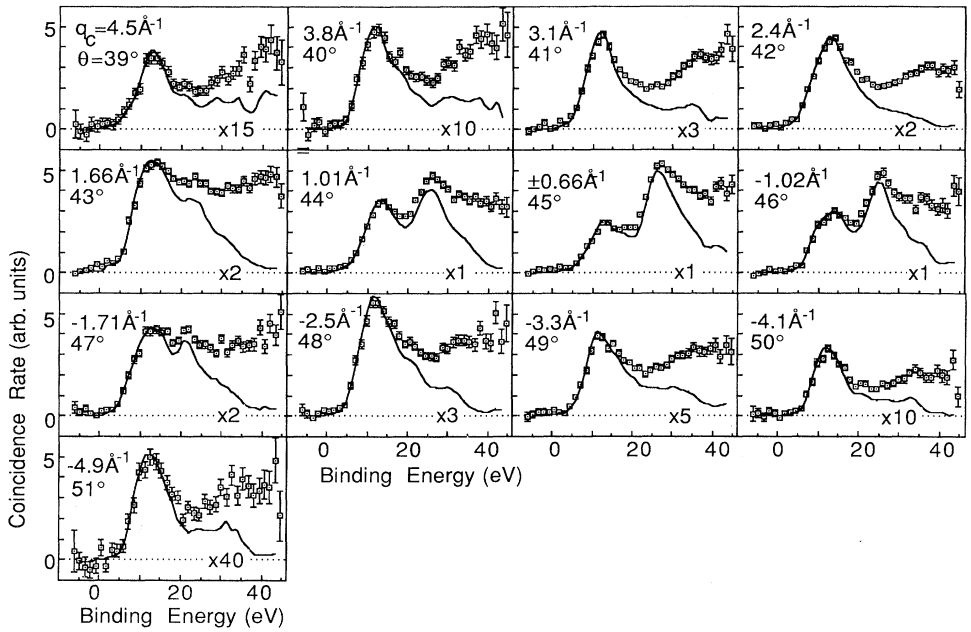

FIG. 4. Spectral momentum map for an evaporated carbon foil, 110 Å thick. The lines were the result of deconvoluting single-channel energy losses from the coincidence spectra. The scattered angle and corrected momenta are recorded with each spectrum.

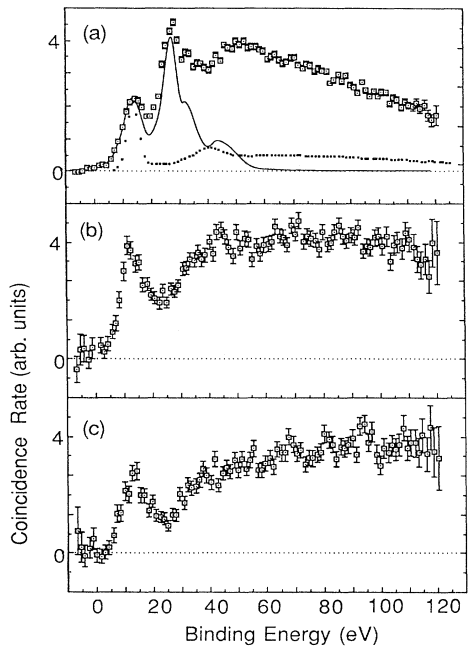

FIG. 5. The extended binding-energy spectra for an evaporated carbon foil 110 Å thick, at symmetric scattered angles of (a) 45° (q_c=0.66 Å^{1}), (b) 41° (q_c=3.8 Å^{-1}), and (c) 50° (q_c=−4.1 Å^{-1}). The solid curve in (a) was the result of deconvoluting the multiple-scattered energy smearing function shown dotted.

of 6 eV FWHM and 0.5 Å^{-1} FWHM two bands were clearly identifiable. The first showed a nondispersing band at about 9 eV below the Fermi energy, while the second revealed a parabolic dispersion with a minimum at q=1.0 Å^{-1} and a binding energy of 23 eV. From Fig. 4 the Fermi energy would appear to be located at a measured energy of about 4.3 eV, which gives good agreement between results. Further, the second peak as a function of increasing binding momentum magnitude moves towards lower binding energies and monotonically decreases in height. The first peak is stationary in binding energy with a local minimum at 45°. Tentatively, from the momentum densities, we describe the first valence state as P like and the second as S like with free-electron dispersion.

The raw data are affected by multiple-scattering events, whose effects grow as the measured binding energy is increased. This is clearly seen in the energy profiles of Fig. 5, which investigate binding energies below the valence band at three different measured momenta. Past the valence band we would expect no significant structure. These detected events, for the most part, can be attributed to the energy-straggling collisions discussed earlier. This is demonstrated by deconvoluting the estimated smearing function from the raw data. The resultant solid curve shown in Fig. 5(a) tends toward zero intensity after the bottom of the valence band. Besides the primary valence peaks, however, there are two further peaks that are most likely related to an incomplete deconvolution. The separation distance of these peaks is again close to 13 eV, which suggests they are satellites of the primary band structure. We cannot, however, discount the possibility of multielectron states or diamondlike bonded band

structure. The lowest diamond band should exist close to the shoulder at 32 eV. It is interesting to note that the binding-energy tail turns down at progressively higher energies as the measured momentum magnitude increases. This is a result of more probable momentum events (i.e., a q closer to zero) undergoing a number of multiple collisions and being scattered into the less intense momentum stations. The effect is outside the valence band and does not significantly contribute to the features observed in this region.

The solid lines in Fig. 4 represent the deconvoluted valence-band spectra obtained from the van Cittert technique. For a comparison of relative peak heights the deconvoluted curves have been replotted in a three-dimensional format in Fig. 6. Little is known about the energy-level scheme in an amorphous solid. Carbon in crystalline form has two common bonding schemes, diamond and graphite. From other work[26] the bonding in evaporated carbon is largely graphitic. The single-channel energy-loss measurements (see Fig. 1) on this carbon sample reveals that the bonding is predominantly graphitic. The spectrum shows the existence of a π-plasmon peak at 7.5 eV, which occurs only in the graphite form of carbon. The position of the $\sigma+\pi$ volume plasmon at 26 eV is also consistent with graphite[22] at 27 eV rather than diamond, which occurs at the higher energy of 31 eV. In theory, close to the center of the Brillouin zone, the long-wavelength states are dependent on an averaged crystal structure that will be similar to amorphous carbon.[23] It would be expected that the band structure of crystalline graphite would then match the energy-level scheme of amorphous carbon at low measured momentum. Away from the zone center, the locally varying bonded network is likely to modify the band relations. For polycrystalline samples the measured band structure is an average over all crystal orientations. If the band map is strongly anisotropic this will cause the measured bands to widen away from the zone center. A broadening of individual bands with increasing measured momentum is also expected for amorphous materials. The degree of short-range order will influence this effect, with trends in dispersion following the similarly bonded crystal.

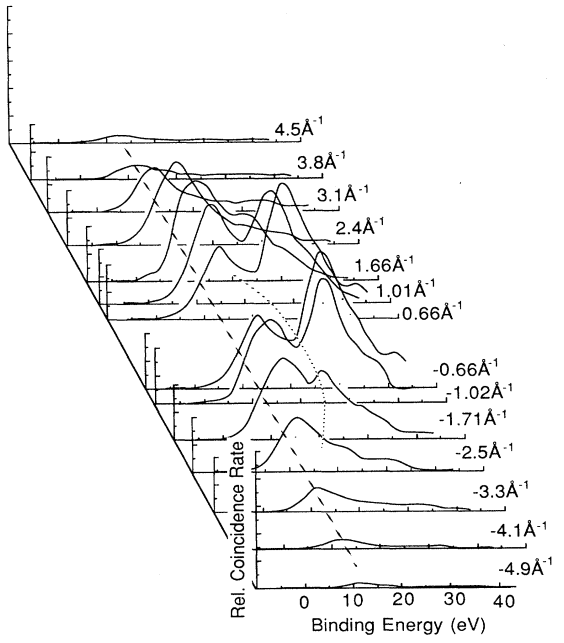

FIG. 6. The deconvoluted curves of Fig. 4 redisplayed in a three-dimensional format. Note that $q_c = 0.66$ Å^{-1} has been repeated at positive and negative values.

The deconvoluted spectra place the two major peaks at 12.8 and 26.2 eV for analyzer positions of $\theta_e = \theta_s = 45°$, respectively. The lower band intensity is more clearly shown as a function of measured momentum. A Gaussian curve-fitting procedure was performed on the deconvoluted data. The primary band structure was closely fitted by two Gaussians of identical width 8.9 ± 0.4 eV FWHM. The tail structure was also fitted with two Gaussians of the same width to account for their influence on the primary band. For momentum magnitudes above 2.4 Å^{-1} it was impossible to separate the two peaks without employing some prior knowledge. For the higher momenta of $|q| > 3.0$ Å^{-1} the Gaussian width had to be progressively reduced to about 7.4 ± 0.4 FWHM to obtain a reasonable fit. The trend is the reverse of the earlier prediction. This may be related to the band-edge intensity being close to the Fermi energy; there is, however, no indication of broadening of the band. The fitted Gaussian's FWHM is nearly twice the measured instrumental resolution. The cause is most likely either an inability to resolve closely space bands or an averaging over a single dispersive band by a wide pass momentum. In the case of the first peak, which appears to be only slightly dispersive, it would be assumed that this is composed of several states. The second peak does disperse; however, its width does not increase from the minimum dispersion position. To help identify the contribution of a wide momentum resolution, the analyzer's acceptance angle was reduced to give a calculated momentum resolution of 0.4 Å^{-1} FWHM. The new data repeated the structure found in the earlier experiments, with poorer statistics due to the reduced coincidence rate. In particular, the relative intensities of the two peaks did not significantly change, which would not have been expected with strong S- and P-orbital characters. The width of the second peak was marginally sharpened but other differences were within the momentum errors quoted above. The amorphous character of the foil did seem to be blurring the band structure.

A comparison of structure close to zero measured momentum between the amorphous carbon data of Ritter *et al.*[3] and our data in Fig. 7 shows close agreement between the positions and relative intensities of the two peaks after Ritter's energy scale is moved by 5.25 eV onto the present scale. We have allowed also for a probable momentum offset in Ritter's data which he describes as between 0 and 1 Å^{-1}. The symmetry of his data suggests a systematic offset of about 0.6 Å^{-1}. The comparison is conducted between the nearest pair of momentum positions in each study. At low measured momenta good

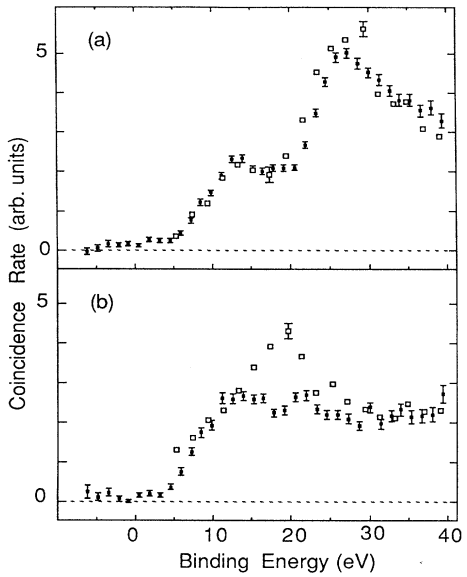

FIG. 7. The comparison of coincidence data for amorphous carbon between that presented here (■) and Ritter *et al.* (Ref. 3) (□) at 25 keV. Ritter mentions a probable systematic offset, which we estimate to be about 0.6 Å^{-1}. For this reason a comparison with the nearest momentum spectra is performed at (a) $q=0$ Å^{-1} (i.e., $q_c=0.66$ Å^{-1}) with 1 Å^{-1} and (b) $q=-1.6$ Å^{-1} (i.e., $q_c=-1.7$ Å^{-1}) with -2.0 Å^{-1}, where the first stated momentum belongs to this study and the second to Ritter *et al.*

agreement exists between the positions and relative intensities of the two peaks. Differences exist at higher measured momenta where Ritter's lower dispersing band appears to maintain a slowly declining intensity over about 3 Å^{-1}. This picture suggests that most of the intensity, where the bands merge at higher momentum, is derived from the lower band. The trend indicated by the present data is that the lower valence state declines rapidly over this range, with the upper band being the major contributor at higher binding momenta. The intensity of the energy spectrum drops rapidly after 3.0-Å^{-1} magnitude measured momentum. The discrepancies do not appear to lie within the experimental errors of either study. The target preparation is a possible answer with the bonding structure or degree of crystallinity being different in the two foils. In our case, the foil after the $(e,2e)$ probe gave no indication of electron-beam-induced recrystallization through sampling the foil using an electron microscope and analyzing its diffraction pattern. The difference in energies of the two probes may also contribute through different sampling depths with the solid target.

In general the foil behaved like nonoriented graphite, with the energy levels approximately corresponding to theoretical self-consistent calculations[24] shown in Fig. 8. Close to zero measured momentum the upper band would then be a composite of the π and σ_2 and σ_3 bands and the lower peak equated to the σ_1 bands. The momentum densities for these bands in crystalline graphite have also been calculated.[4] The σ bands are formed from the trigonal planar bonding electrons, the remaining p_z orbitals generate the two π bands. For symmetry reasons the momentum density of the π bands must drop to zero in the basal plane of the crystal. The π and upper σ bands have zero momentum density at $q=0$ Å^{-1} and are said to be *P*-like, while the lower bands are *S*-like with a maximum at the center of the Brillouin zone. The major attributes of the spherically averaged crystal structure fit the data. A possible exception is that the major band gap is filled even at the lowest momentum data. This may be a result of elastic scattering not deconvoluted from the data which yields a small background related to higher momentum states.

The comparison with graphite is further justified by the $(e,2e)$ experimental results obtained from a thin graphite foil, as shown in Fig. 9. The foil, prepared to an estimated average thickness of 170 Å, was investigated using the previous experimental energy and momentum resolutions of 4.5 eV and 0.9 Å^{-1}, respectively. At about $q=0$ Å^{-1} the coincidence count rate dropped to about 1 count/sec with an accidental coincidence count rate of 6 counts/sec into a wider background window of 275 nsec. The raw data had a similar form to that of amorphous carbon close to the center of the zone, with peaks located at 13.2 and 26.2 eV. The second peak lies on the rising background of satellite counts from the first state. The tail at higher binging energies has a greater intensity in this thicker sample because of the increased probability of multiple inelastic scattering. Away from $q=0$ Å^{-1} the structure follows the predicted atomiclike bonding along the *c* axis, with both bands remaining dispersionless. The upper band closely reflects the amorphous carbon band at these resolutions. Graphite's lower band declines rapidly in intensity with increasing momentum as with amorphous carbon, but does not appear to disperse. This behavior agrees with the calculated momentum density in this direction, which also monotonically decreases. The correspondence between theory and experiment for parallel momentum densities is shown in Fig. 10. The theoretical momentum densities[4] have been folded with a 0.9-Å^{-1} FWHM Gaussian. For comparison we have assumed that the momentum density parallel to the basal plane is constant within the analyzer resolution. The expected analyzer aperture momentum offset perpendicular to the *c* axis was about 0.4 Å^{-1}. The data are extracted from the plots with the assumption that the peak widths do not vary and that the inelastic background at the lower peak position is a constant fraction of the initial peak's height. The fraction of 0.1 ± 0.05 is obtained from the wide momentum position. These assumptions were used since the plasmon loss becomes anisotropic to the incoming and outgoing directions, which complicates the deconvolution procedure. The wide momentum resolution does sample the band structure off the ideal Γ-*A* axis, which partly describes the peak widths (about 4–5 eV) and nonzero intensity of the first peak at the 45° position. It is also worth mentioning that with the probe sampling close to the exit side of the foil that surface roughness may be contributing to the observed discrepancies.

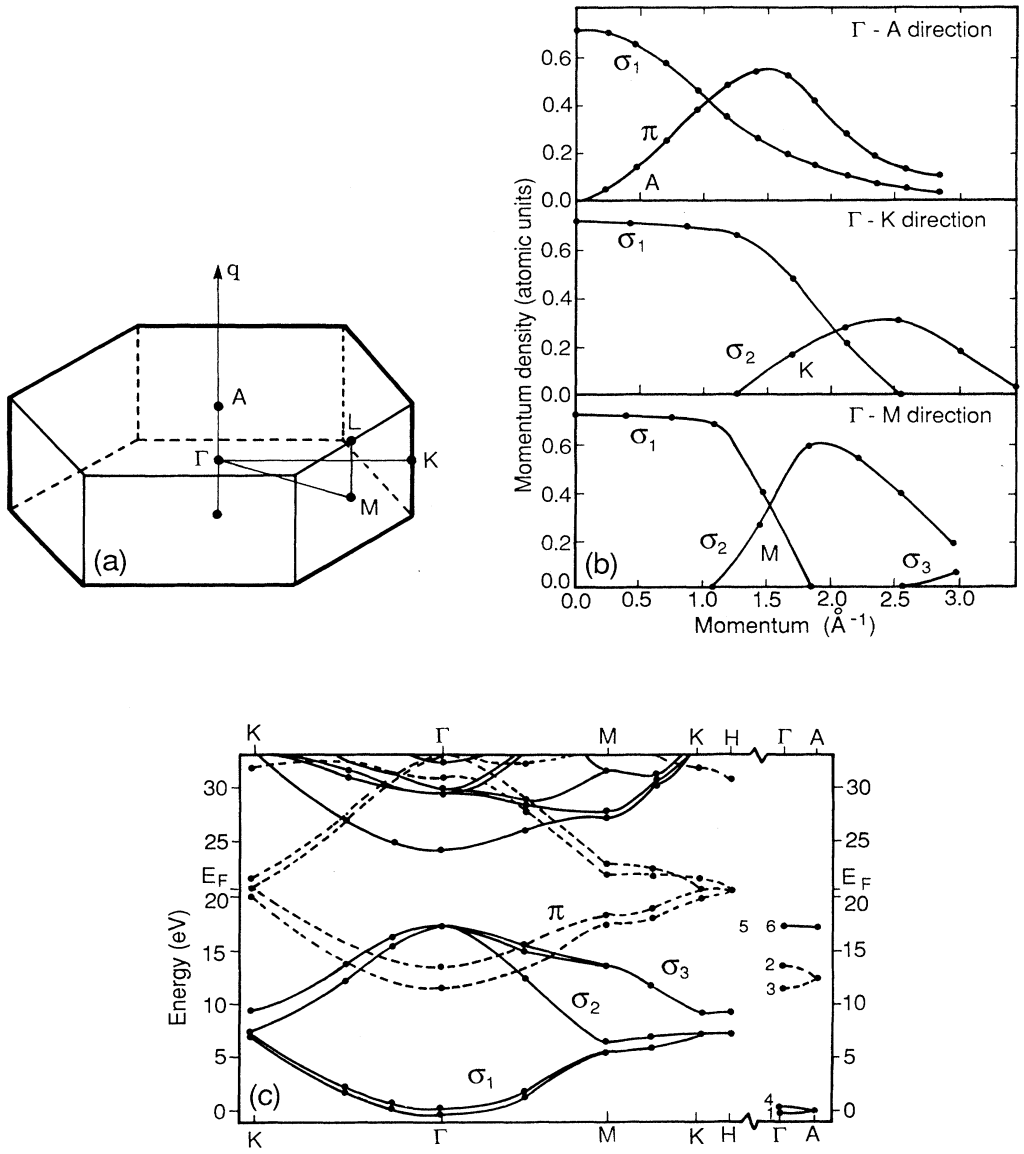

FIG. 8. The first Brillouin zone for graphite is displayed in (a) and the electronic band map in this zone along the high-symmetry directions is shown in (b) and (c). The map has been obtained from Holzwarth *et al.* (Ref. 24).

B. Aluminum and aluminum oxide foils

Evaporated 130-Å-thick aluminum foils have been studied by us[1] under conditions similar to those of amorphous carbon. The spectra covered a similar range of momenta and energies and revealed two valence peaks situated at 13 and 30 eV. These states were dispersionless and their intensities indicated that the upper state was *P*-like, while the lower state was *S*-like. By taking into account the target-depth sampling profile of the $(e,2e)$ probe and the distribuion of oxide within the foil, it is likely that most of the signal was derived from the oxide rather than the aluminum metal. The nondispersing lower band did not correspond to the free-electron-like band of aluminum. The results, for this reason, were compared to the band map of crystalline α alumina with the view that the amorphous oxide should approximate it close to zero measured momentum. The upper valence structure is composed of many closely spaced bands which are relatively dispersionless. The band itself splits into contributions from the O $2p$ lone pair orbitals (0–2 eV from the top of the band) and the hybridization of the oxygen-aluminum orbitals (2–6 eV), with the major component being the O $2p$ orbitals. The lower dispersionless bands range in energy from 16 to 19 eV below the topmost band, which agrees with the experimental separation. The character of this band is *S*-like with bonding contributions from the O $2s$ and Al $3s$–O $2s$ orbitals,

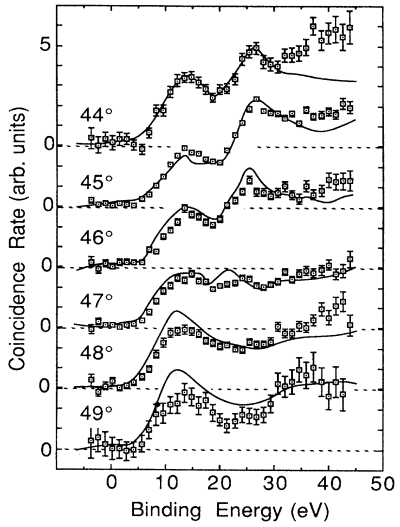

FIG. 9. The comparison of raw data collected from amorphous carbon, represented by the solid line, and the graphite data points. Both were recorded in equivalent experimental conditions.

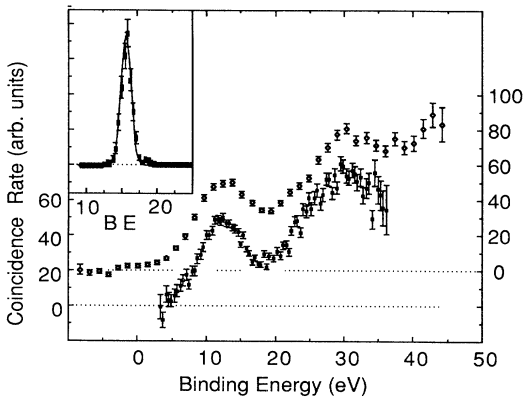

FIG. 11. The results from an aluminum foil (130 Å thick) at two different energy resolutions (◇) 4.5 eV FWHM and (■) 1.5 eV for a scattered angle of 45° and a fixed momentum resolution. The measured resolution of 1.5 eV FWHM from the argon $3p$ state is shown in the inset.

again agreeing with the experimental results.

In this study, the measurement has been repeated at the analyzer position of 45° with the improved measured energy resolution of 1.5 eV FWHM. The momentum resolution was maintained at 0.9 $Å^{-1}$ FWHM. The intention was to resolve the upper valence structure into two bands described above, which experimental x-ray photoemission spectroscopy density-of-states studies on

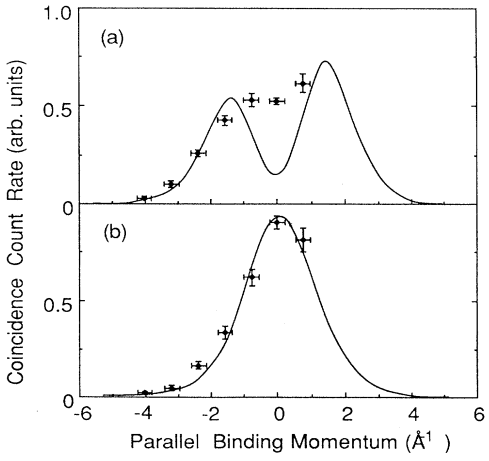

FIG. 10. Coincident rate as a function of parallel binding momentum for the two dispersionless bands at (a) 13.2 eV and (b) 26.2 eV. The curves are the theoretical momentum densities (Ref. 4) for the π and σ_1 bands, respectively, along the c axis, folded with a 0.9-$Å^{-1}$ FWHM resolution and Mott scattering term. Both plots have been normalized by the same factor.

α-alumina crystals have shown[25] to have a separation of about 4 eV. The data, however, repeated the structure from the earlier study as shown in Fig. 11, with the notable exception of the minima, which appear to deepen at this energy resolution, and a small upward energy shift, which locates the peaks at 11.3 and 29.5 eV. The shift is related to the improved resolution and being able to define the absolute energy within ±0.25 eV. The first peak, however, does not reveal any sign of splitting into two distributions. This may be an outcome of the amorphous characteristic smoothing out the valence-band structure, especially due to surfacelike band states. A small contribution from surface carbon may also smooth out the distribution at this energy position.

VIII. CONCLUSION

The foils studied here revealed well-defined structure in the valence region which approximately agreed with similar bonded crystalline forms. In particular, for amorphous carbon close to zero measured target momentum, the binding-energy loss spectra were in good agreement with that of oriented graphite, with the peak positions at 12.8 and 26.2 eV. Earlier studies by Ritter and Gao enabled us to compare for the first time data obtained by independent $(e,2e)$ technique on solids. Good agreement was found close to zero target momentum, but the distribution did appear to change at higher momenta. The amorphous data presented here followed an atomic momentum density distribution with the lower band structure showing a concave dispersion.

From this experiment at these energies, it is evident that single-channel collisions are a major factor in the data analysis and that multiple-scattering events cause a reduction in the total coincidence signal and the appearance of satellite events. A possible advantage of the measurements, as with Auger measurements, is that at low

probe energies the surface becomes the major source of detected (e,2e) reactions in the valence region, even in the symmetric transmission mode. To avoid the multiple events for the investigation of bulk spectral momentum maps in low atomic number foils prepared around 100 Å, the beam energy would need to be about 50 keV. The 17-fold decrease in signal, because of a reduced (e,2e) differential cross section, should be compensated by the increased probability of being able to detect single scattering events. Work in this direction is continuing.

ACKNOWLEDGMENTS

The support of the Australian Research Grants Scheme (ARGS) and the University of Western Australia is gratefully acknowledged. Dr. M. A. Bennett contributed significantly to the early stages of this work.

[1]P. Hayes, M. A. Bennett, J. Flexman, and J. F. Williams, Rev. Sci. Instrum. **59**, 2445 (1988).
[2]R. Camilloni, A. Giardandi Guidoni, R. Tiribelli, and G. Stefani, Phys. Rev. Lett. **29**, 618 (1972).
[3]A. L. Ritter, J. R. Dennison, and R. Jones, Phys. Rev. Lett. **53**, 2054 (1984).
[4]C. Gao, A. L. Ritter, J. R. Dennison, and N. A. W. Holzwarth, Phys. Rev. B **37**, 3914 (1988).
[5]H. Ehrhardt, K. Jung, G. Knoth, and P. Schlemmer, Z. Phys. D **1**, 3 (1986).
[6]V. G. Levin, V. G. Neudatchin, and Yu. F. Smirnov, Phys. Status Solidi **49**, 48 (1972).
[7]V. G. Neudatchin, G. A. Novoskol'tseva, and Yu. F. Smirnov, Zh. Eksp. Teor. Fiz. **55**, 1039 (1969) [Sov. Phys.—JETP **28**, 540 (1969)].
[8]B. I. Lundqvist, Phys. Kondens. Mater. **6**, 193 (1967); **6**, 206 (1967); **7**, 117 (1968); **9**, 236 (1969).
[9]V. G. Neudachin and F. A. Zhivpistsev, Phys. Rev. Lett. **32**, 995 (1974).
[10]F. A. Zhivopistsev and F. E. Comas, Fiz. Tverd. Tela **21**, 924 (1979) [Sov. Phys.—Solid State **21**, 541 (1979)].
[11]F. A. Zhivopistsev and F. E. Comas, Phys. Status Solidi B **100**, 303 (1980).
[12]L. J. Allen, I. E. McCarthy, V. W. Maslen, and C. J. Rossouw, Aust. J. Phys. (to be published).
[13]H. Raether, Springer Tracts Mod. Phys. **88**, 362 (1980).
[14]N. Ishigure, C. Mori, and T. J. Watanbae, Phys. Soc. Jpn. **44**, 1196 (1978).
[15]J. C. Ashley, J. J. Cowan, R. H. Ritchie, V. E. Anderson, and J. Hoezel, Thin Solid Films **60**, 361 (1979).
[16]R. Jones and A. L. Ritter, J. Electron Spectrosc. **40**, 285 (1986).
[17]H. J. Fitting and J. Reinhardt, Phys. Status Solidi A **88**, 245 (1985).
[18]P. H. van Cittert, Z. Phys. **211**, 39 (1931).
[19]P. Hayes, M. A. Bennett, J. Flexman, and J. F. Williams, Phys. Rev. B **38**, 13 371 (1988).
[20]I. E. McCarthy and E. Weigold, Phys. Rep. **27C**, 275 (1976).
[21]M. Oberlin, M. Onerlin, and M. Maubios, Philos. Mag. **32**, 833 (1975).
[22]W. Y. Liang and S. L. Cundy, Philos. Mag. **18**, 251 (1969).
[23]J. M. Ziman, J. Phys. C **4**, 3129 (1971).
[24]N. A. W. Holzwarth, S. G. Louie, and S. Rabii, Phys. Rev. B **26**, 5382 (1982).
[25]S. P. Kowalsky, F. R. Freely, L. Ley, V. T. Gritsyna, and D. A. Shirley, Solid State Commun. **23**, 161 (1977).